catalysts

MDPI

Article

Atomically Dispersed Pd Sites on ZrO_2 Hybridized N-Doped Carbon for Efficient Suzuki–Miyaura Reaction

Jiaqi Du [1], Yidan Peng [1], Xu Guo [1], Guoliang Zhang [1,2,3], Fengbao Zhang [1,2,3], Xiaobin Fan [1,2,3], Wenchao Peng [1,2,3] and Yang Li [1,2,3,*]

[1] School of Chemical Engineering and Technology, Tianjin University, Tianjin 300354, China
[2] Haihe Laboratory of Sustainable Chemical Transformations, Tianjin 300192, China
[3] Institute of Shaoxing, Tianjin University, Zhejiang 312300, China
* Correspondence: liyang1895@tju.edu.cn

Abstract: Researchers studying heterogeneous catalysis are intrigued by single-atom catalysts (SACs) due to their ultrahigh atomic utilization. However, only a few reports on SAC-catalyzed classical organic transformations are available. In this work, atomically dispersed Pd sites are confined to a ZrO_2 hybridized N-doped carbon skeleton with a smart design. UiO-66-NH_2 is used to anchor Pd atoms by the coordination of the donor atoms including lone pairs of electrons and metal atoms. Subsequently, the in situ introduction of ZrO_2 doping is achieved using pyrolysis, which helps improve the catalytic performance by modulating the electronic state. The Pd@ZrO_2/N–C catalyst obtained from the unique design exhibits a high yield (99%) in eco-friendly media with an extremely low noble metal dosage (0.03 mol% Pd) for the Suzuki reaction. Moreover, Pd@ZrO_2/N–C remains highly active after being reused several times and possesses versatility in a variety of substrates. This strategy offers a feasible alternative to designing SACs with atomically dispersed noble metals for heterogeneous reactions.

Keywords: palladium; heterogeneous catalyst; Suzuki reaction; ZrO_2 doping; N-doped carbon

Citation: Du, J.; Peng, Y.; Guo, X.; Zhang, G.; Zhang, F.; Fan, X.; Peng, W.; Li, Y. Atomically Dispersed Pd Sites on ZrO_2 Hybridized N-Doped Carbon for Efficient Suzuki–Miyaura Reaction. *Catalysts* **2023**, *13*, 651. https://doi.org/10.3390/catal13040651

Academic Editors: Victorio Cadierno and Carl Redshaw

Received: 13 February 2023
Revised: 21 March 2023
Accepted: 22 March 2023
Published: 25 March 2023

1. Introduction

C–C coupling reactions are versatile methods to carry out organic syntheses, which arouse extensive attention from academic research and industrial applications [1–4]. The palladium (Pd)-catalyzed Suzuki reaction is a potent technique for constructing C–C bonds [5–8]. Pd complex-based homogeneous catalysts have extremely high catalytic performance. However, they are often hard to reuse due to their time-consuming and energy-intensive complex separation process [9–11]. Such flaws can be fixed with heterogeneous catalysts decorated by Pd nanoparticles [12–18]. However, as only a minority of noble metal atoms can become the catalytic sites, their metal utilization is lower compared with homogeneous catalysts [19,20]. Consequently, it should be crucial to create heterogeneous catalysts with maximum atomic utilization from the economic and environmental perspectives.

Single-atom catalysts (SACs) are novel developments in heterogeneous catalysis [21,22], offering the advantages of homogeneous (maximum metal utilization) and heterogeneous (facile separation) catalysts together [23]. However, the isolated single atoms in SACs tend to aggregation and deactivation because of their high surface energy [24,25]. Presently, one of the most effective ways to deal with these challenges is to prepare N-doped carbon (N–C) supports [26–28] to confine metal atoms, in particular, metal–organic framework (MOF)-derived N–C carriers.

It has been shown that MOF-derived carbon materials are excellent supports for SACs [29–33]. The most common technique for producing SACs is pyrolysis, which involves the high-temperature thermal decomposition of suitable precursors [34–36]. In

general, when metal nodes are atomically dispersed in MOFs, they may be pyrolyzed and reduced in situ to prepare transition metal SACs. However, such a method is hardly effective for noble metals, which are infrequently used as metal nodes during the preparation of MOFs [37]. In addition, such catalysts are mostly confined to electrochemical catalysis [38–40].

Herein, a new composite material (Pd@ZrO_2/N–C) consisting of Pd single atoms confined on zirconium dioxide (ZrO_2) hybridized with N-doped carbon is validated to be a promising catalyst for the Suzuki reaction. UiO-66-NH_2, a widely used and thermally stable zirconium (Zr)-based MOF, is selected as the matrix for hosting Pd atoms. The free coordination –NH_2 functional groups, can adsorb metal precursors and further coordinate with the single noble metal atoms. Furthermore, ZrO_2 doping can be introduced in situ with the pyrolysis of the Zr-based MOF, which facilitates the regulation of the electronic state at single active sites, resulting in better catalytic performance. Specifically, Pd^{2+} ions are adsorbed on UiO-66–NH_2 with hydrothermal synthesis. After pyrolysis, the Pd atoms are individually dispersed and well distributed on the ZrO_2-hybridized support. Thanks to the distinctive atom-isolated structure and the electronic state regulation of single-atom active sites, Pd@ZrO_2/N–C demonstrates superior catalytic activity and universality of various substrates for the Suzuki reaction in an aqueous solution. In addition, Pd@ZrO_2/N–C can be reused with satisfactory catalytic performance.

2. Results and Discussion

2.1. Synthesis of Pd@ZrO_2/N–C

The synthesis of Pd@ZrO_2/N–C is depicted in Scheme 1. $PdCl_2$ is used as the metal precursor to adsorb Pd^{2+} ions onto the skeleton of UiO-66–NH_2 using a self-assembly process. The corresponding complex resulting from the adsorption process is named $PdCl_2$/UiO-66–NH_2. Within this case, the uncoordinated –NH_2 can act as the Lewis base to immobilize the metal atom, thus the Pd^{2+} ions can be coordinated with the nitrogen atoms for the formation of metal–N bonds. Following pyrolysis at 700 °C under a flowing nitrogen atmosphere, the Pd sites are immobilized on in situ ZrO_2-hybridized nitrogen-doped carbon to generate the Pd@ZrO_2/N–C catalyst.

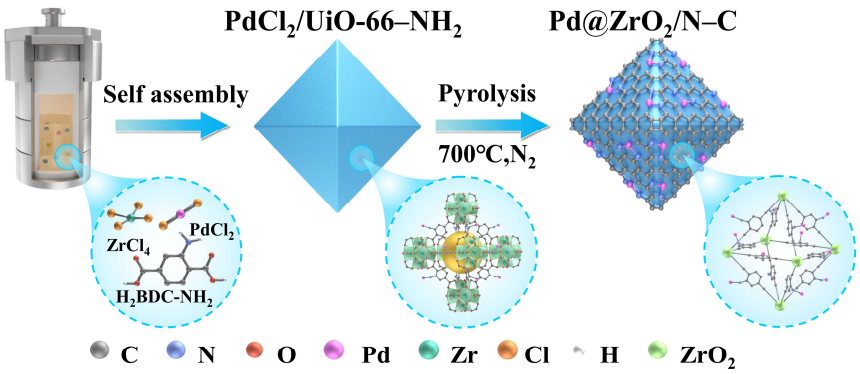

Scheme 1. Schematic representation of the synthesis process for Pd@ZrO_2/N–C.

2.2. Characterization of the Catalysts

Compared to pristine UiO-66–NH_2, the color of the materials changes from yellow to gray after the addition of $PdCl_2$, indicating strong electrostatic adsorption between the Pd^{2+} ions and the –NH_2 groups (Figure S1) [41]. All prepared materials present the characteristic peaks at 2θ = 7.5° and 8.5° in X-ray diffraction (XRD) patterns (Figure S2a) following self-assembly, which corresponds to the characteristic peaks of UiO-66. This is very consistent with earlier studies [42,43], demonstrating the preservation of MOF crystallinity and structure after the adsorption process. Fourier transform infrared (FT-IR) spectroscopy (Figure S3) is applied to further validate the interaction of the $PdCl_2$ precursor with UiO-66–NH_2. The analysis implies that the scissoring vibration in N–H

is responsible for the absorption peak at 1495 cm^{-1}, whereas the stretching vibration in C–N accounts for the peaks at 1098 as well as 1156 cm^{-1} [44]. The decrease in peak intensity after Pd^{2+} adsorption suggests that the $–NH_2$ groups may play a major part in the adsorption of Pd^{2+} ions [45]. After pyrolysis, it is clear from the XRD patterns of Pd@ZrO_2/C and Pd@ZrO_2/N–C that the characteristic reflection peaks of ZrO_2 appear (Figure S2b). Furthermore, the pattern of Pd@ZrO_2/C shows the characteristic diffraction peaks belonging to Pd. The development in Pd nanoparticles is indicated by the peak at 40.1°, which is associated with the (111) plane of Pd. In contrast, as for Pd@ZrO_2/N–C, there are no diffraction peaks attributable to the Pd metal, excluding the aggregation and formation of large Pd nanoparticles. This provides proof that the uncoordinated $–NH_2$ groups have a crucial role in stabilizing the $PdCl_2$ precursors and further hindering their assembly during pyrolysis. The diffraction peaks in ZrO_2 vanish from the pattern of Pd/N–C (Figure S2b) following acid etching, verifying that the added HF solution successfully removed the ZrO_2 nanoparticles.

The morphology of the catalysts is analyzed using a series of tests. The transmission electron microscopy (TEM) and scanning electron microscopy (SEM) images (Figures 1a and S4–S6) show that the samples retain their initial octahedral structure after adsorption and pyrolysis. The elemental mapping results (Figure 1b) verify that the elements are distributed uniformly in Pd@ZrO_2/N–C. The high-angle annular dark-field scanning transmission electron microscopy (HAADF-STEM) image (Figure 1c) of Pd@ZrO_2/N–C displays the isolated Pd atoms (labeled with green circles). The high-resolution transmission electron microscopy (HRTEM) image of Pd@ZrO_2/N–C (Figure S7a) demonstrates the distribution of ZrO_2 nanoparticles on the substrate, while the images of Pd/N–C (Figure S8) show that the prepared material retains the octahedral morphology and removes ZrO_2.

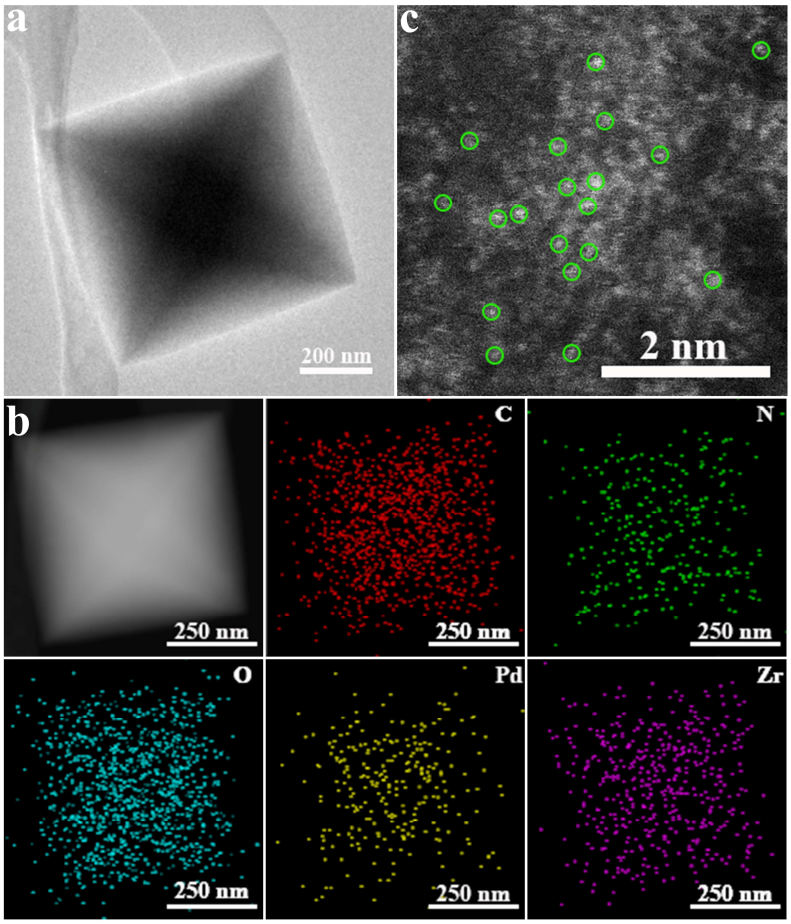

Figure 1. (**a**) TEM, (**b**) EDS elemental mapping, and (**c**) HAADF-STEM image of Pd@ZrO_2/N–C.

The coordination states of the elements including C, N, Zr, O, and Pd are analyzed using X-ray photoelectron spectroscopy (XPS). The deconvolution in the C 1s peak of ZrO_2/N–C leads to five components at 284.9, 285.8, 286.2, 287.0, and 288.9 eV, which can be assigned to C=C, C–N, C–O, N–C=O, and C=O bonds, respectively (Figure S9a) [46]. C–N and N–C=O appear, which proves that N has been doped on the support. Contrasted with ZrO_2/N–C, the amounts of those groups in Pd@ZrO_2/N–C descend (Figure S9c) probably due to the generation of Pd–N bonds, which could be assisted with the state analysis of N. The N 1s spectrum for ZrO_2/N–C (Figure S10a) displays the binding energy peaks at 398.5 eV of pyridinic N, 400.3 eV of pyrrolic N, and 401.3 eV of graphitic N [47]. In comparison to ZrO_2/N–C, the spectra of Pd@ZrO_2/N–C and Pd/N–C display one new peak at 399.3 eV, which indicates that metal–nitrogen bonds are formed as a result of some N configuration coordinated to the metal sites (Figure S10b,c) [41]. Furthermore, it can also be observed that the introduction of Pd metal increases the intensity of pyrrolic N as well as pyridinic N given that the π-conjugated structure can accept the p-electron from both varieties of N atoms, which are usually regarded as the coordination sites for the atomically dispersed Pd [48].

The Zr 3d XPS spectrum of Pd@ZrO_2/N–C (Figure S11) gives the binding energy of Zr $3d_{5/2}$ (182.4 eV), which is inferior to the previously reported value (182.8 eV) [49]. The downfield change of 0.4 eV of Zr in Pd@ZrO_2/N–C indicates a notable electron transfer between the Zr center and Pd metal or the skeleton. Additionally, the binding energy of O 1s (Figure S12a) could give further insight into the coordination state of the materials. The peak at 530.2 eV (O_M) arises from combinations of O connecting with metal atoms. Evidence for oxygen vacancies is shown by a peak at 531.8 eV (O_V). Other weakly bound oxygen species, such as H_2O and hydroxyl, are responsible for the peak at 533.6 eV (O_H) [50]. It can be shown that a significant increase in the intensity of O_V appears after introducing Pd metal from the spectra of Pd@ZrO_2/N–C and ZrO_2/N–C (Figure 2a,b), indicating that additional oxygen vacancies are produced, which is further verified with Electron Paramagnetic Resonance (EPR). The results of EPR (Figure 2d) demonstrate a signal induced by oxygen vacancies formation at g = 2.003. The total spin number under quantitative conditions is from 8.372×10^{16} to 9.909×10^{16} when the Pd metal is introduced, indicating an augment of oxygen vacancies, which is identical to the XPS results. This is probably due to the generation of Pd–O by the electron-transfer process between Pd and ZrO_2 during the annealing in N_2. The Pd content decreased from 3.27 mol% to 0.15 mol% (determined with XPS) after the removal of ZrO_2, which also indicates that some Pd atoms are loaded on ZrO_2 with an established metal–support interaction.

The interaction is further verified with the change in specific surface area (SSA) and ZrO_2 particle. SSA is measured with Brunauer–Emmett–Teller (BET) at 42.4 m^2/g for Pd@ZrO_2/N–C as well as 8.9 m^2/g ZrO_2/N–C (Figure S13). The HRTEM images demonstrate that the size of ZrO_2 in the Pd@ZrO_2/N–C catalyst (Figure S7b) is 3.4 nm on average, while it is 5.2 nm in ZrO_2/N–C (Figure S14). These findings imply that the larger the size of the ZrO_2 nanoparticles, the smaller the SSA of the catalyst. It can also be assumed that the growth of ZrO_2 nanoparticles is responsible for the reduction in SSA. Conversely, it could be speculated that the existence of Pd atoms can suppress the particle growth of ZrO_2 during the pyrolysis treatment by converting the O–Zr species on the surface to the Pd–O species, which gives Pd@ZrO_2/N–C a larger surface area. This provides more evidence for the interaction between Pd and ZrO_2. After the removal of ZrO_2 with washing, there is only one fitting peak referring to O_H in the O 1s spectrum of Pd/N–C (Figure S12b), which verifies the absence of metal–O bonds. The Pd 3d XPS spectrum (Figure S15a) reveals the two peaks associated with Pd^{2+} $3d_{3/2}$ (343.0 eV) and $3d_{5/2}$ (337.9 eV) [51]. As for Pd@ZrO_2/C and Pd@ZrO_2/N–C (Figures S15b and 2d), the Pd 3d signal is shielded by the Zr 3p signal. Nevertheless, inductively coupled plasma mass spectroscopic (ICP-MS) analysis reveals that the contents of Pd in Pd@ZrO_2/C and Pd@ZrO_2/N–C are 0.5 wt% and 0.3 wt%, respectively, confirming the existence of Pd in both of the samples.

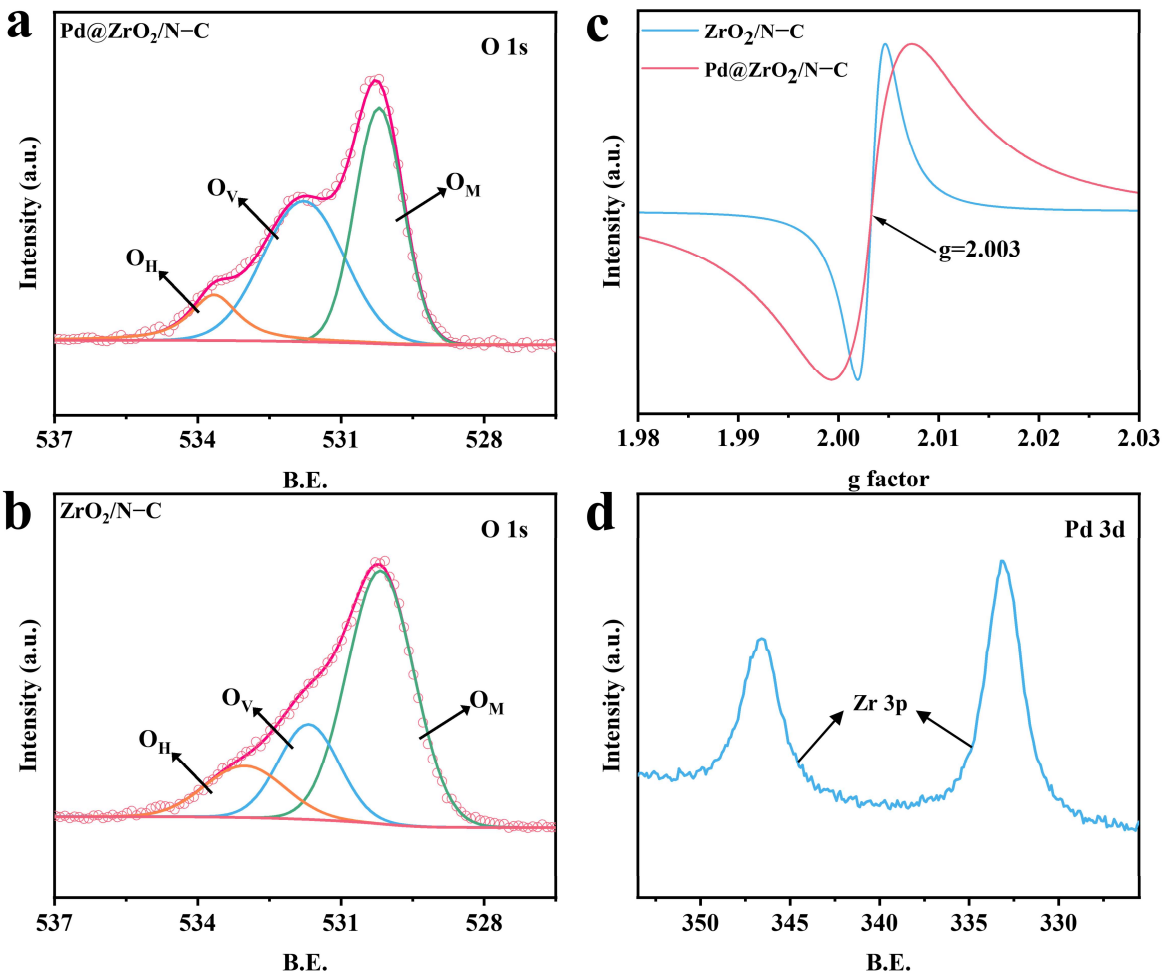

Figure 2. (**a**) O 1s XPS spectrum of Pd@ZrO_2/N–C. (**b**) O 1s XPS spectrum of ZrO_2/N–C. (**c**) EPR signals of oxygen vacancies in ZrO_2/N–C and Pd@ZrO_2/N–C, respectively. (**d**) Pd 3d XPS spectrum of Pd@ZrO_2/N–C.

The coordination states of Pd within Pd@ZrO_2/N–C are further validated with X-ray absorption spectroscopy (XAS). The X-ray absorption near-edge structure (XANES) spectra suggest that the absorption threshold for Pd@ZrO_2/N–C lies between Pd foil and PdO (Figure 3a). It shows that Pd is positively charged. The Fourier-transformed extended XAFS (FT-EXAFS) spectrum of Pd@ZrO_2/N–C (Figure 3b) displays a single peak at 1.5 Å, which is in accordance with the Pd–O scattering pair [52]. No Pd–Pd coordination features of the Pd foil reference are observed in Pd@ZrO_2/N–C, proving that the Pd atoms exist in isolation. The local structure parameters are further obtained with least squares EXAFS fitting (Figures S16 and S17) and summarized in Table S1. The results reveal that the Pd atom may be anchored by three O or N atoms at a mean bond length of about 2.0 Å in Pd@ZrO_2/N–C. The results of the wavelet transform (WT) are illustrated in Figure 3c. For Pd@ZrO_2/N–C, there is one WT maximum at ~5 $Å^{-1}$, which coincides with the Pd–O bonding in the PdO plot. No additional signals can be identified, which is quite consistent with the findings of previous analyses. To sum up, the results presented above demonstrate that the Pd single-atom catalyst with ZrO_2-hybridized N–C supports is successfully synthesized.

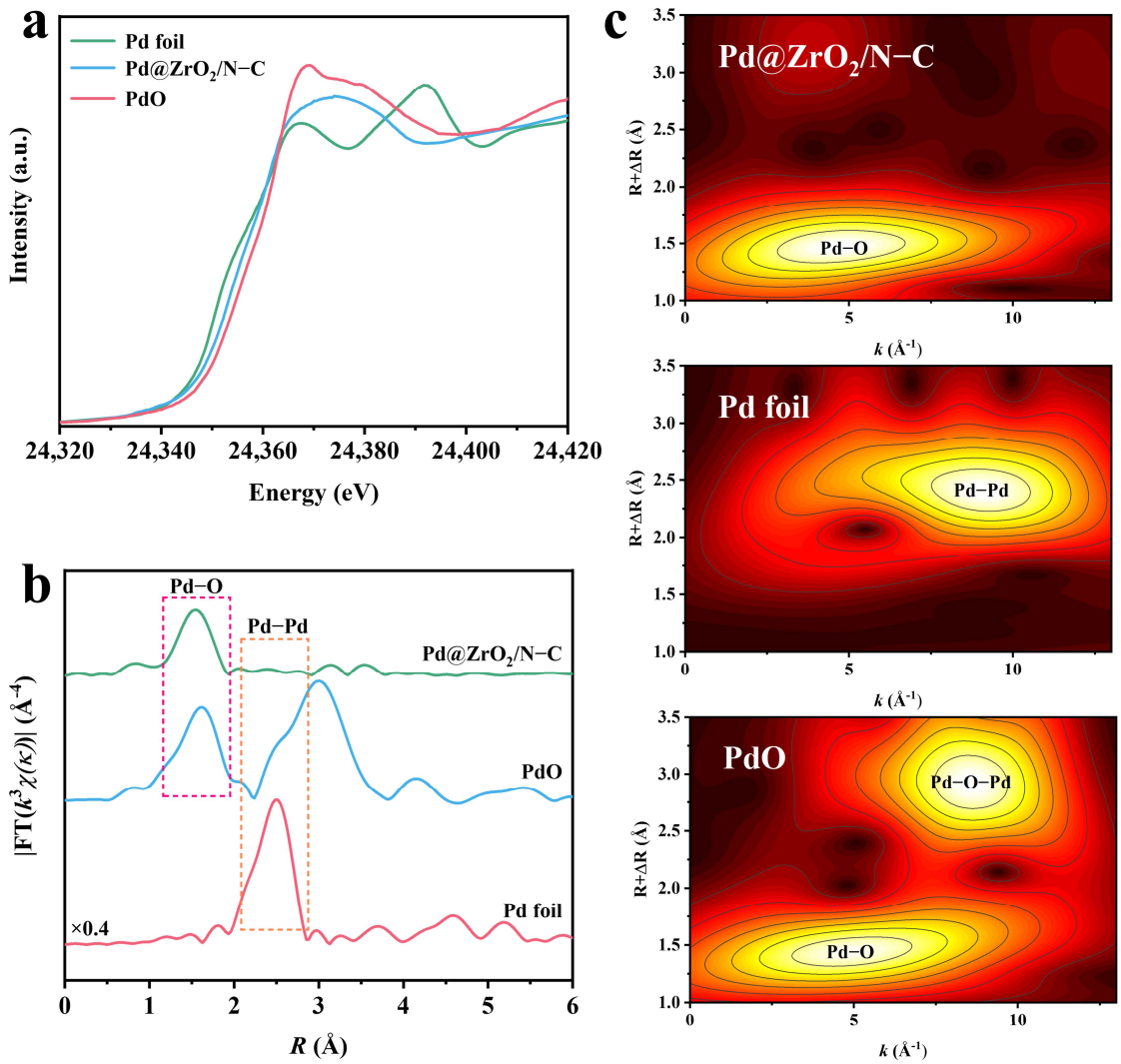

Figure 3. (**a**) XANES spectra of referenced materials and Pd@ZrO_2/N–C for the Pd K-edge. (**b**) The k^3-weighted Fourier transforms of Pd K-edge EXAFS spectra for Pd@ZrO_2/N–C and referenced materials. (**c**) WT for Pd@ZrO_2/N–C, Pd foil, and PdO, respectively.

2.3. Performance Evaluation of the Suzuki Reaction

For optimal reaction conditions, variables including reaction time, temperature, catalyst loadings, and bases are explored. To increase the solubility of the substrate, an equal volume of ethanol is mixed into water as a solvent. In a range of 2 h to 4 h, the yield increases from 61% to 99% (Table 1, entries 1–3). At this time, the turnover frequency (TOF) value reaches 825 h^{-1}, which is more efficient than most reported single-atom Pd catalysts applied to Suzuki coupling (Table S2). The yield raises with the reaction temperature acceleration (60 °C to 80 °C) from 50% to 99% (Table 1, entries 3–5). Considering that a further increase in the reaction temperature will reach the azeotropic point of the system and a prolonged reaction time will raise the operating cost, the suitable reaction time and reaction temperature are 4 h and 80 °C, respectively. The amount of the catalyst is also critical, so the effect of different amounts of catalyst (Pd content of the molar ratio of substrates) on the reaction is tested. Without the aid of the catalyst, the coupling product is negligible (Table 1, entry 12). However, the catalytic activity rises with the increasing amount of catalyst, reaching 99% yield with 0.03 mol% Pd (Table 1, entries 3, 6, and 7). This may be due to the existence of more active sites. Considering that a further increase in catalyst dosage would be cost-prohibitive and that the catalytic yield has already reached a very high level, a Pd content of 0.03 mol% is determined to be the optimum catalyst amount.

Under these optimum reaction circumstances, the effects of four commonly used bases (K_2CO_3, Na_2CO_3, KOH, NaOH) on the reaction are investigated (Table 1, entries 3 and 8–10). The reaction yields involving such bases are all above 90%, which indicates that the effect of the base is insignificant. K_2CO_3 is more appropriate for the reaction due to the best catalytic activity in its presence and its weak causticity. Furthermore, in the absence of the base, there are almost no products (Table 1, entry 11). The best reaction yield is obtained using a mixture of H_2O and EtOH (1:1) solution containing a catalyst of Pd@ZrO_2/N–C (0.03 mol% Pd) and a base of K_2CO_3 at 80 °C for 4 h. Furthermore, no coupling product is observed using ZrO_2/N–C as the catalyst for the control experiment. This demonstrates that the reaction is cannot take place without Pd.

Table 1. Suzuki reactions for a wide variety of conditions with Pd@ZrO_2/N–C [a].

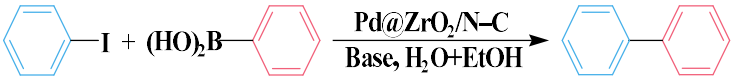

Entry	mol% (Pd)	Base	Temp. (°C)	Time (h)	Yield [b] (%)
1	0.03	K_2CO_3	80	2	61
2	0.03	K_2CO_3	80	3	82
3	0.03	K_2CO_3	80	4	99
4	0.03	K_2CO_3	60	4	50
5	0.03	K_2CO_3	70	4	93
6	0.01	K_2CO_3	80	4	82
7	0.02	K_2CO_3	80	4	94
8	0.03	Na_2CO_3	80	4	94
9	0.03	KOH	80	4	90
10	0.03	NaOH	80	4	95
11	0.03	—	80	12	Trace
12	—	K_2CO_3	80	12	Trace

[a] Reaction condition: 0.5 mmol of iodobenzene, 0.6 mmol of phenylboronic acid, 1.5 mmol of the base, 2 mL of solvent (H_2O:EtOH = 1:1), Pd@ZrO_2/N–C (0.01 mol%–0.03 mol%) at various temperatures (°C). [b] GC yield.

To prove the superiority of isolated atoms as well as the merits of the introduction of ZrO_2 doping in the supports, other prepared catalysts are also evaluated. The Pd@ZrO_2/C catalyst with the same Pd equivalent weight has a biphenyl yield of 79% under the same conditions (Figure 4a). Because Pd nanoparticles develop in Pd@ZrO_2/C, it is less active than Pd@ZrO_2/N–C. Specifically, Pd active sites in Pd@ZrO_2/N–C are exposed on the surface, while those in Pd@ZrO_2/C are occluded inside the Pd nanoparticles. The disclosure of Pd atoms enhances the atom's utilization coefficient and favors the catalytic performance. This demonstrates the superiority of SACs. Similarly, the Pd/N–C (the content of Pd is 1.25 wt% determined with XPS) catalyst obtained after the removal of ZrO_2 exhibited poor catalytic performance with a yield of only 5%. This result demonstrates the positive effects of ZrO_2 doping. The whole reaction pathway usually consists of three main steps (Figure 4b) [53,54]. The catalyst has been shown to act as the donor of the charge within the oxidative addition process. The Zr ions can donate lone pair electrons to the Pd sites in Pd@ZrO_2/N–C and boost the electron transfer [55], which enhances the catalyst's capacity to donate charges and makes the oxidative addition process more efficient. Subsequently, at the time of transmetallation and reductive elimination, the catalyst acts as the acceptor of the charge. Resulting from the electron transfer to the adjacent ZrO_2, the Pd single-atom sites are positively charged, which facilitates the steps of transmetallation and reductive elimination by acting as electron acceptors [56]. Therefore, this strongly confirms the significant advantage of the ZrO_2 in the supports.

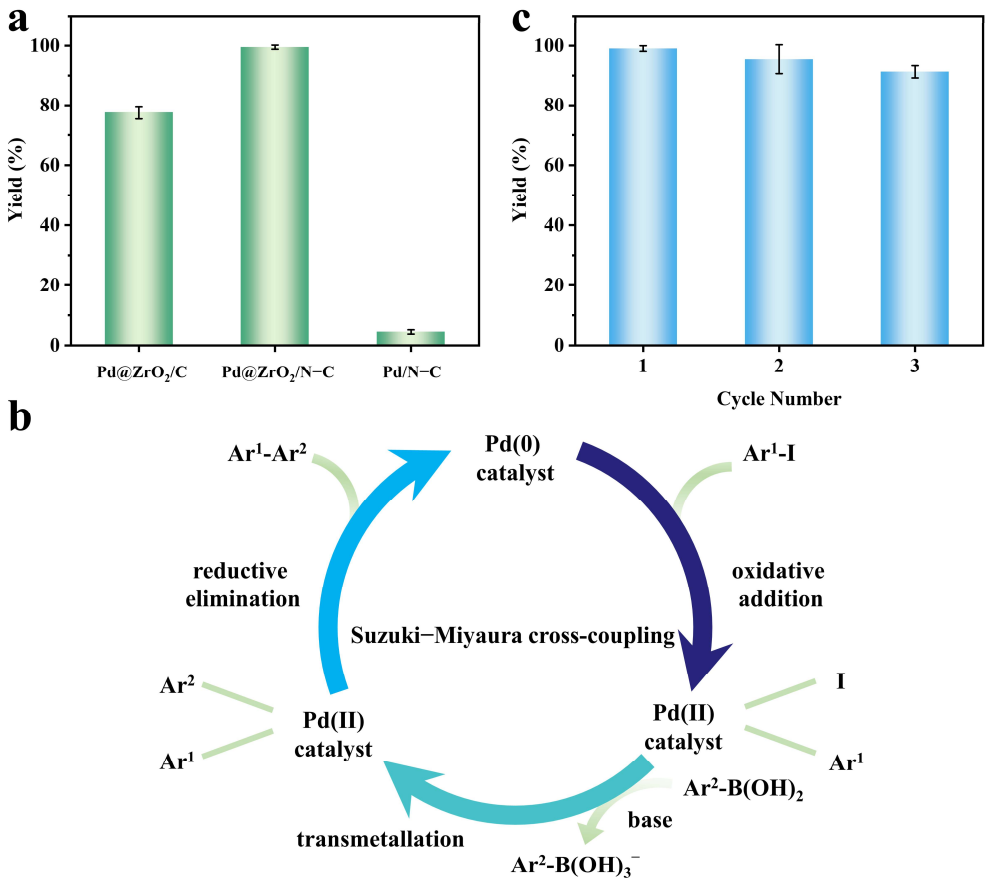

Figure 4. (**a**) Catalytic performance toward the Suzuki reaction over different catalysts. (**b**) Schematics of the Suzuki reaction. (**c**) Recyclability of Pd@ZrO_2/N–C for the Suzuki reaction.

The recyclability of Pd@ZrO_2/N–C is another evaluation index that should be further assessed (Figure 4c). After the reaction, Pd@ZrO_2/N–C is recovered with centrifugation and then dried after being washed with DI water. The dried powder is collected for a new reaction cycle. The test repeats for three consecutive cycles. Pd@ZrO_2/N–C is used for three runs and the yield remains above 91%, showing no significant loss of catalytic ability. To evaluate the amount of Pd leached from Pd@ZrO_2/N–C after each reaction cycle, the solution (10 mL) obtained by removing the Pd catalyst after the reaction is tested using ICP-MS. The concentration of Pd in the supernatant is 0.024, 0.005, and 0.011 ppm, which are equivalent to 1.59 mol%, 0.32 mol%, and 0.76 mol% of the Pd quantity in the catalyst, respectively. These results indicate that the leaching level is extremely low, which is why the catalytic activity could be maintained.

On the other hand, the universality of the catalysts with various substituted aryl halides and arylboronic acids is also tested. The use of various substrates with different groups obtains excellent isolated yields (Table 2). Pd@ZrO_2/N–C is well tolerated by multifarious groups on the substrates, including methyl (**3b**–**3d**), cyano (**3e**), nitro (**3f**), and ether (**3g**). The reaction of aryl iodides obtains a higher yield than that of aryl bromides (**3a**) because of the relatively high activity of iodides. Steric hindrance also affects the catalytic reaction. For iodotoluene, the highest yield is obtained for para-substitution, which is superior to that of ortho-substituted and meta-substituted iodotoluene for the same reaction time (**3b**–**3d**). Overall, the catalyst exhibits superior catalytic performance across an extensive variety of substrates.

Table 2. Suzuki reactions of various substituted aryl halides and arylboronic acids [a].

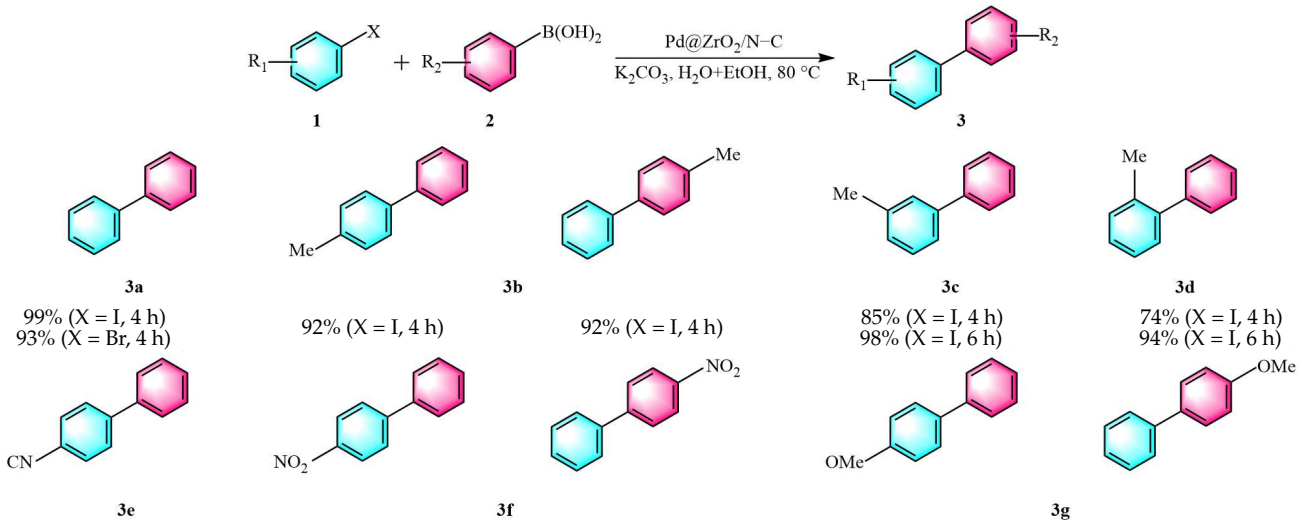

[a] Reaction condition: 0.5 mmol of aryl halide, 0.6 mmol of arylboronic acid, 1.5 mmol of K_2CO_3, 2 mL of solvent (H_2O:EtOH = 1:1), Pd@ZrO_2/N–C (0.03 mol%) at 80 °C. GC yields were reported.

3. Materials and Methods

3.1. Chemicals

Zirconium chloride ($ZrCl_4$, 98%), palladium chloride (Pd, 59–60%), 2-aminoterephthalic acid (H_2BDC-NH_2, 98%), N, N-dimethylformamide (DMF, 99.5%), potassium carbonate (K_2CO_3, 99%), acetic acid (HAc, 99.5%) and magnesium sulfate anhydrous ($MgSO_4$, 99%) were obtained from Shanghai Aladdin Biochemical Technology Co., Ltd. (Shanghai, China). Absolute ethanol (EtOH, 99.7%) and methanol (MeOH, 99.9%) were purchased from Jiangtian Chemical Technology Co., Ltd. (Tianjin, China). Deionized (DI) water was used throughout the process of the experiments.

3.2. Synthesis of $PdCl_2$/UiO-66–NH_2

$PdCl_2$ (250 µL, 1mg/mL DMF), $ZrCl_4$ (85.6 mg, 0.36 mmol), and H_2BDC-NH_2 (66.5 mg, 0.36 mmol) were added in 80 mL DMF mixed with 9.6 mL HAc in a 100 mL glass vial. A 100 mL Teflon-lined autoclave was used to pack the mixed solution after 30 min of sonication. Next, following sealing, the autoclave was put into a preheated oven. The oven was set to 120 °C, and the process took 24 h. Then, the product was centrifugated and washed 3 times with a mixed solution (MeOH:DMF = 1:4). The powder was collected for subsequent use after drying at 90 °C.

3.3. Synthesis of Pd@ZrO_2/N–C

The powder was loaded into a tube furnace. Under a flowing nitrogen atmosphere, $PdCl_2$/UiO-66–NH_2 was heated to 700 °C at 5 °C/min and subsequently maintained at this condition for another 3 h. The black powder was collected once it cooled to room temperature for subsequent characterization and catalytic testing. For comparison, the ZrO_2/N–C catalyst without Pd, the Pd@ZrO_2/C catalyst without N doping, and the Pd/N–C catalyst without ZrO_2 were also prepared. The supporting information describes the specific methods of synthesis.

3.4. Suzuki–Miyaura Cross-Coupling Reaction

Unless otherwise noted, the Suzuki reaction was carried out as follows: a typical procedure is to disperse the Pd@ZrO_2/N–C catalyst (equivalent weight 0.03 mol% Pd) in a flask with 1 mL DI water as well as 1 mL ethanol. The solution was then supplemented with iodobenzene (103 mg, 0.5 mmol), K_2CO_3 (209.4 mg, 1.5 mmol), and phenylboronic acid

(75 mg, 0.6 mmol). The catalytic reaction took place in the oil bath under constant stirring at a temperature of 80 °C under an air atmosphere. The reaction duration was 4 h. Following the reaction, ethyl acetate (2 mL × 3) was used to extract the corresponding products, which were then dried with magnesium sulfate anhydrous ($MgSO_4$) and analyzed using a gas chromatography (GC) system.

4. Conclusions

In conclusion, the single-atom catalyst named Pd@ZrO_2/N–C is successfully synthesized using the in situ pyrolysis of UiO-66–NH_2 adsorbed with Pd^{2+} ions. The anchoring of Pd atoms on ZrO_2-hybridized N-doped C is confirmed with various characterization methods. Such an original structure design utilizes the interaction between isolated atom active sites and supports, resulting in synthesized materials with splendid catalytic performance. It is demonstrated that Pd@ZrO_2/N–C exhibits excellent activity for the Suzuki reaction in an environmentally friendly solution with high yields, good universality, and no significant decline in catalytic performance after reuse. Overall, this catalyst benefits from the unique structural design based on MOF. This study offers novel perspectives on the design of SACs for efficient heterogeneous catalysis.

Supplementary Materials: The following supporting information can be downloaded at: https://www.mdpi.com/article/10.3390/catal13040651/s1, characterization, other synthetic procedures, Figure S1: The color of UiO-66–NH_2 and $PdCl_2$/UiO-66–NH_2; Figure S2: XRD patterns of (a) UiO-66, UiO-66–NH_2, $PdCl_2$/UiO–66, and $PdCl_2$/UiO-66–NH_2 and (b) Pd@ZrO_2/C, Pd@ZrO_2/N–C, and Pd/N–C, respectively; Figure S3: FT-IR spectra of UiO-66–NH_2 and $PdCl_2$/UiO-66–NH_2, respectively; Figure S4: TEM images of (a) and (b) UiO-66, (c) and (d) UiO-66–NH_2, (e) and (f) $PdCl_2$/UiO-66, and (g) and (h) $PdCl_2$/UiO-66–NH_2; Figure S5: SEM image of Pd@ZrO_2/N–C; Figure S6: TEM images of (a) and (b) Pd@ZrO_2/C, (c) and (d) ZrO_2/N–C; Figure S7: (a) HRTEM image and (b) the statistic diagram of ZrO_2 particle sizes of the Pd@ZrO_2/N–C sample; Figure S8: (a) TEM image and (b) HRTEM image of Pd/N–C; Figure S9: C 1s XPS spectra of (a) ZrO_2/N–C, (b) Pd@ZrO_2/C, (c) Pd@ZrO_2/N–C, and (d) Pd/N–C, respectively; Figure S10: N 1s XPS spectra of (a) ZrO_2/N–C, (b) Pd@ZrO_2/N–C, and (c) Pd/N–C, respectively; Figure S11: Zr 3d XPS spectrum of Pd@ZrO_2/N–C; Figure S12: O 1s XPS spectra of (a) Pd@ZrO_2/C and (b) Pd/N–C, respectively; Figure S13: N_2 adsorption/desorption isotherms of (a) Pd@ZrO_2/N–C and (b) ZrO_2/N–C; Figure S14: (a) HRTEM image and (b) the statistic diagram of ZrO_2 particle sizes in the ZrO_2/N–C sample; Figure S15: Pd 3d XPS spectra of (a) Pd/N–C and (b) Pd@ZrO_2/C, respectively; Figure S16: (a) EXAFS R space fitting curve (circles) and the experimental data (blue line) of Pd@ZrO_2/N–C, and (b) EXAFS k space fitting curve (circles) and the experimental data (blue line) of Pd@ZrO_2/N–C; Figure S17: (a) EXAFS R space fitting curve (circles) and the experimental data (blue line) of Pd foil, and (b) EXAFS k space fitting curve (circles) and the experimental data (blue line) of Pd foil; Table S1: EXAFS fitting parameters at the Pd K-edge for various samples ($S_0{}^2$ = 0.818). Table S2: Comparison of the turnover frequencies reported over palladium catalysts in the Suzuki coupling.

Author Contributions: Conceptualization, J.D.; formal analysis, J.D.; investigation, J.D.; writing—original draft preparation, J.D.; writing—review and editing, J.D., Y.P., X.G. and Y.L.; supervision, G.Z., W.P. and Y.L.; funding acquisition, F.Z., X.F. and Y.L. All authors have read and agreed to the published version of the manuscript.

Funding: This research was funded by the Specialized Research Funds for the National Natural Science Foundation of China, grant number nos. 22078242 and U20A20153, Innovative Research Group Project of the National Natural Science Foundation of China grant number No. 22121004, and Haihe Laboratory of Sustainable Chemical Transformations, grant number CYZC202107.

Data Availability Statement: Data are contained within the article and Supplementary Material.

Conflicts of Interest: The authors declare no conflict of interest.

References

1. Biffis, A.; Centomo, P.; Del Zotto, A.; Zecca, M. Pd metal catalysts for cross-couplings and related reactions in the 21st century: A critical review. *Chem. Rev.* **2018**, *118*, 2249–2295. [CrossRef] [PubMed]
2. Pengyao, J.; Shujie, W.; Qing, S.; Xiaodong, L.; Ziqian, L.; Guanghua, L.; Qiaolin, W. Salen–porphyrin-based conjugated microporous polymer supported Pd nanoparticles: Highly efficient heterogeneous catalysts for aqueous C–C coupling reactions†. *J. Mater. Chem. A* **2019**, *7*, 2660–2666.
3. Trzeciak, A.M.; Augustyniak, A.W. The role of palladium nanoparticles in catalytic C–C cross-coupling reactions. *Coord. Chem. Rev.* **2019**, *384*, 1–20. [CrossRef]
4. Chen, Z.; Vorobyeva, E.; Mitchell, S.; Fako, E.; Ortuno, M.A.; Lopez, N.; Collins, S.M.; Midgley, P.A.; Richard, S.; Vile, G.; et al. A heterogeneous single-atom palladium catalyst surpassing homogeneous systems for Suzuki coupling. *Nat. Nanotechnol.* **2018**, *13*, 702–707. [CrossRef] [PubMed]
5. Yanhui, W.; Xiaotian, Q.; Qiao, M.; Peng, L.; Gavin Chit, T. Stereoselective palladium-catalyzed base-free Suzuki–Miyaura cross-coupling of tetrasubstituted *gem*-difluoroalkenes: An experimental and computational study. *ACS Catal.* **2021**, *11*, 4799–4809.
6. Wang, L.; Lyu, S.; Zhang, P.; Tian, X.; Wang, D.; Huang, W.; Liu, Z. Nitrogen-bonded ultrasmall palladium clusters over the nitrogen-doped carbon for promoting Suzuki cross-coupling reactions. *Adv. Compos. Hybrid Mater.* **2022**, *5*, 1396–1403. [CrossRef]
7. Beletskaya, I.P.; Alonso, F.; Tyurin, V. The Suzuki-Miyaura reaction after the nobel prize. *Coord. Chem. Rev.* **2019**, *385*, 137–173. [CrossRef]
8. Alonso, F.; Beletskaya, I.P.; Yus, M. Non-conventional methodologies for transition-metal catalysed carbon–carbon coupling: A critical overview. Part 2: The Suzuki reaction. *Tetrahedron* **2008**, *64*, 3047–3101. [CrossRef]
9. Molnár, Á.; Papp, A. Catalyst recycling—A survey of recent progress and current status. *Coord. Chem. Rev.* **2017**, *349*, 1–65. [CrossRef]
10. Wan, Y.; Wang, H.; Zhao, Q.; Klingstedt, M.; Terasaki, O.; Zhao, D. Ordered mesoporous Pd/silica–carbon as a highly active heterogeneous catalyst for coupling reaction of chlorobenzene in aqueous media. *J. Am. Chem. Soc.* **2009**, *131*, 4541–4550. [CrossRef]
11. Cho, J.K.; Najman, R.; Dean, T.W.; Ichihara, O.; Muller, C.; Bradley, M. Captured and cross-linked palladium nanoparticles. *J. Am. Chem. Soc.* **2006**, *128*, 6276–6277. [CrossRef]
12. Wang, J.; Li, T.; Zhao, Z.; Zhang, X.; Pang, W. Pd nanoparticles embedded into MOF-808: Synthesis, structural characteristics, and catalyst properties for the Suzuki–Miyaura coupling reaction. *Catal. Lett.* **2021**, *152*, 1545–1554. [CrossRef]
13. Veisi, H.; Ozturk, T.; Karmakar, B.; Tamoradi, T.; Hemmati, S. In situ decorated Pd NPs on chitosan-encapsulated Fe_3O_4/SiO_2-NH_2 as magnetic catalyst in Suzuki-Miyaura coupling and 4-nitrophenol reduction. *Carbohydr. Polym.* **2020**, *235*, 115966. [CrossRef]
14. Xinyao, S.; Ning, S.; Wengang, L.; Manhong, L.; Jian, L. In situ generation of supported palladium nanoparticles from a Pd/Sn/S chalcogel and applications in 4-nitrophenol reduction and Suzuki coupling†. *J. Mater. Chem. A* **2019**, *7*, 4446–4450.
15. Matías, B.; Dario, M.; Cristina, T.; Andrea, B.; Denis, B.; Paolo, P.; Michal, O.; Aristides, B.; Zhibo, L.; Wencai, R.; et al. Palladium nanoparticles supported on graphene acid: A stable and eco-friendly bifunctional C–C homo- and cross-coupling catalyst. *Green Chem.* **2019**, *21*, 5238–5247.
16. Feizi Mohazzab, B.; Jaleh, B.; Issaabadi, Z.; Nasrollahzadeh, M.; Varma, R.S. Stainless steel mesh-GO/Pd NPs: Catalytic applications of Suzuki–Miyaura and Stille coupling reactions in eco-friendly media. *Green Chem.* **2019**, *21*, 3319–3327. [CrossRef]
17. Baran, T.; Nasrollahzadeh, M. Facile synthesis of palladium nanoparticles immobilized on magnetic biodegradable microcapsules used as effective and recyclable catalyst in Suzuki-Miyaura reaction and *p*-nitrophenol reduction. *Carbohydr. Polym.* **2019**, *222*, 115029. [CrossRef]
18. Li, Y.; Fan, X.; Qi, J.; Ji, J.; Wang, S.; Zhang, G.; Zhang, F. Palladium nanoparticle-graphene hybrids as active catalysts for the Suzuki reaction. *Nano Res.* **2010**, *3*, 429–437. [CrossRef]
19. Kim, S.; Jee, S.; Choi, K.M.; Shin, D.-S. Single-atom Pd catalyst anchored on Zr-based metal-organic polyhedra for Suzuki-Miyaura cross coupling reactions in aqueous media. *Nano Res.* **2020**, *14*, 486–492. [CrossRef]
20. He, P.; Xu, B.; Xu, X.; Song, L.; Wang, X. Surfactant encapsulated palladium-polyoxometalates: Controlled assembly and their application as single-atom catalysts. *Chem. Sci.* **2016**, *7*, 1011–1015. [CrossRef]
21. Cao, C.; Song, W. Single-atom catalysts for thermal heterogeneous catalysis in liquid: Recent progress and future perspective. *ACS Mater. Lett.* **2020**, *2*, 1653–1661. [CrossRef]
22. Wang, A.Q.; Li, J.; Zhang, T. Heterogeneous single-atom catalysis. *Nat. Rev. Chem.* **2018**, *2*, 65–81. [CrossRef]
23. Liu, D.; He, Q.; Ding, S.; Song, L. Structural regulation and support coupling effect of single-atom catalysts for heterogeneous catalysis. *Adv. Energy Mater.* **2020**, *10*, 2001482. [CrossRef]
24. Gawish, M.; Drmosh, Q.; Onaizi, S. Single atom catalysts: An overview of the coordination and interactions with metallic supports. *Chem. Rec.* **2022**, *22*, e202100328. [CrossRef]
25. Jeong, H.; Shin, S.; Lee, H. Heterogeneous atomic catalysts overcoming the limitations of single-atom catalysts. *ACS Nano* **2020**, *14*, 14355–14374. [CrossRef]
26. Wang, X.; Jia, Y.; Mao, X.; Liu, D.; He, W.; Li, J.; Liu, J.; Yan, X.; Chen, J.; Song, L.; et al. Edge-rich Fe–N_4 active sites in defective carbon for oxygen reduction catalysis. *Adv. Mater.* **2020**, *32*, 2000966. [CrossRef]
27. Zhang, H.; Li, J.; Xi, S.; Du, Y.; Hai, X.; Wang, J.; Xu, H.; Wu, G.; Zhang, J.; Lu, J.; et al. A graphene-supported single-atom FeN_5 catalytic site for efficient electrochemical CO_2 reduction. *Angew. Chem. Int. Ed.* **2019**, *58*, 14871–14876. [CrossRef]

28. Gong, W.; Lin, Y.; Chen, C.; Al-Mamun, M.; Lu, H.S.; Wang, G.; Zhang, H.; Zhao, H. Nitrogen-doped carbon nanotube confined Co–N_x sites for selective hydrogenation of biomass-derived compounds. *Adv. Mater.* **2019**, *31*, 1808341. [CrossRef]
29. Zhou, D.; Li, X.; Shang, H.; Qin, F.; Chen, W. Atomic regulation of metal–organic framework derived carbon-based single-atom catalysts for the electrochemical CO_2 reduction reaction. *J. Mater. Chem. A* **2021**, *9*, 23382–23418. [CrossRef]
30. Xie, X.; Shang, L.; Xiong, X.; Shi, R.; Zhang, T. Fe single-atom catalysts on MOF-5 derived carbon for efficient oxygen reduction reaction in proton exchange membrane fuel cells. *Adv. Energy Mater.* **2021**, *12*, 2102688. [CrossRef]
31. Sui, X.; Zhang, L.; Li, J.; Doyle-Davis, K.; Li, R.; Wang, Z.; Sun, X. Advanced support materials and interactions for atomically dispersed noble-metal catalysts: From support effects to design strategies. *Adv. Energy Mater.* **2021**, *12*, 2102556. [CrossRef]
32. Wen, X.; Zhang, Q.; Guan, J. Applications of metal–organic framework-derived materials in fuel cells and metal-air batteries. *Coord. Chem. Rev.* **2020**, *409*, 213214. [CrossRef]
33. Zhao, W.; Wan, G.; Peng, C.; Sheng, H.; Wen, J.; Chen, H. Key single-atom electrocatalysis in metal-organic framework (MOF)-derived bifunctional catalysts. *ChemSusChem* **2018**, *11*, 3473–3479. [CrossRef]
34. Wang, Q.; Ina, T.; Chen, W.-T.; Shang, L.; Sun, F.; Wei, S.; Sun-Waterhouse, D.; Telfer, S.G.; Zhang, T.; Waterhouse, G.I.N. Evolution of Zn(II) single atom catalyst sites during the pyrolysis-induced transformation of ZIF-8 to N-doped carbons. *Sci. Bull.* **2020**, *65*, 1743–1751. [CrossRef]
35. Gong, Y.N.; Jiao, L.; Qian, Y.; Pan, C.; Zheng, L.; Cai, X.; Liu, B.; Yu, S.H.; Jiang, H.L. Regulating the coordination environment of MOF-templated single-atom nickel electrocatalysts for boosting CO_2 reduction. *Angew. Chem. Int. Ed.* **2020**, *59*, 2705–2709. [CrossRef]
36. Yang, Z.K.; Yuan, C.Z.; Xu, A.W. A rationally designed Fe-tetrapyridophenazine complex: A promising precursor to a single-atom Fe catalyst for an efficient oxygen reduction reaction in high-power Zn-air cells. *Nanoscale* **2018**, *10*, 16145–16152. [CrossRef]
37. Song, Z.; Zhang, L.; Doyle-Davis, K.; Fu, X.; Luo, J.L.; Sun, X. Recent advances in MOF-derived single atom catalysts for electrochemical applications. *Adv. Energy Mater.* **2020**, *10*, 2001561. [CrossRef]
38. Liu, K.; Tang, Y.; Yu, Z.; Ge, B.; Ren, G.; Ren, Y.; Su, Y.; Zhang, J.; Sun, X.; Chen, Z.; et al. High-loading and thermally stable $Pt_1/MgAl_{1.2}Fe_{0.8}O_4$ single-atom catalysts for high-temperature applications. *Sci. China Mater.* **2020**, *63*, 949–958. [CrossRef]
39. Zhao, L.; Zhang, Y.; Huang, L.B.; Liu, X.Z.; Zhang, Q.H.; He, C.; Wu, Z.Y.; Zhang, L.J.; Wu, J.; Yang, W.; et al. Cascade anchoring strategy for general mass production of high-loading single-atomic metal-nitrogen catalysts. *Nat. Commun.* **2019**, *10*, 1278. [CrossRef]
40. Zhang, L.; Wang, A.; Wang, W.; Huang, Y.; Liu, X.; Miao, S.; Liu, J.; Zhang, T. Co–N–C catalyst for C–C coupling reactions: On the catalytic performance and active sites. *ACS Catal.* **2015**, *5*, 6563–6572. [CrossRef]
41. Rong, C.; Shen, X.; Wang, Y.; Thomsen, L.; Zhao, T.; Li, Y.; Lu, X.; Amal, R.; Zhao, C. Electronic structure engineering of single-atom Ru sites via Co-N_4 sites for bifunctional pH-universal water splitting. *Adv. Mater.* **2022**, *34*, 2110103. [CrossRef]
42. Chowdhuri, A.R.; Laha, D.; Chandra, S.; Karmakar, P.; Sahu, S.K. Synthesis of multifunctional upconversion NMOFs for targeted antitumor drug delivery and imaging in triple negative breast cancer cells. *Chem. Eng. J.* **2017**, *319*, 200–211. [CrossRef]
43. Rakhshani, N.; Hassanzadeh Nemati, N.; Saadatabadi, A.R.; Sadrnezhaad, S.K. Fabrication of novel poly(*N*-vinylcaprolactam)-coated UiO-66-NH_2 metal organic framework nanocarrier for the controlled release of doxorubicin against A549 lung cancer cells. *J. Drug Delivery Sci. Technol.* **2021**, *66*, 102881. [CrossRef]
44. Kandiah, M.; Nilsen, M.H.; Usseglio, S.; Jakobsen, S.; Olsbye, U.; Tilset, M.; Larabi, C.; Quadrelli, E.A.; Bonino, F.; Lillerud, K.P. Synthesis and stability of tagged UiO-66 Zr-MOFs. *Chem. Mater.* **2010**, *22*, 6632–6640. [CrossRef]
45. Zhao, Y.; Wang, D.; Wei, W.; Cui, L.; Cho, C.W.; Wu, G. Effective adsorption of mercury by Zr(IV)-based metal-organic frameworks of UiO-66-NH_2 from aqueous solution. *Environ. Sci. Pollut. Res. Int.* **2021**, *28*, 7068–7075. [CrossRef]
46. Chen, W.X.; Pei, J.J.; He, C.T.; Wan, J.W.; Ren, H.L.; Wang, Y.; Dong, J.C.; Wu, K.L.; Cheong, W.C.; Mao, J.J.; et al. Single tungsten atoms supported on MOF-derived N-doped carbon for robust electrochemical hydrogen evolution. *Adv. Mater.* **2018**, *30*, 1800396. [CrossRef]
47. Cai, A.; He, H.W.; Zhang, Q.C.; Xu, Y.S.; Li, X.T.; Zhang, F.B.; Fan, X.B.; Peng, W.C.; Li, Y. Synergistic effect of N-doped sp^2 carbon and porous structure in graphene gels toward selective oxidation of C–H bond. *ACS Appl. Mater. Interfaces* **2021**, *13*, 13087–13096. [CrossRef]
48. Wang, Y.; Jia, G.; Cui, X.; Zhao, X.; Zhang, Q.; Gu, L.; Zheng, L.; Li, L.H.; Wu, Q.; Singh, D.J.; et al. Coordination number regulation of molybdenum single-atom nanozyme peroxidase-like specificity. *Chem* **2021**, *7*, 436–449. [CrossRef]
49. Sun, Z.Y.; Zhang, X.R.; Na, N.; Liu, Z.M.; Han, B.X.; An, G.M. Synthesis of ZrO_2-carbon nanotube composites and their application as chemiluminescent sensor material for ethanol. *J. Phys. Chem. B* **2006**, *110*, 13410–13414. [CrossRef]
50. Lu, X.-F.; Wu, D.-J.; Li, R.-Z.; Li, Q.; Ye, S.-H.; Tong, Y.-X.; Li, G.-R. Hierarchical $NiCo_2O_4$ nanosheets@hollow microrod arrays for high-performance asymmetric supercapacitors. *J. Mater. Chem. A* **2014**, *2*, 4706–4713. [CrossRef]
51. Liu, J.; Chen, Z.; Liu, C.; Zhang, B.; Du, Y.; Liu, C.-F.; Ma, L.; Xi, S.; Li, R.; Zhao, X.; et al. Molecular engineered palladium single atom catalysts with an M-C_1N_3 subunit for Suzuki coupling. *J. Mater. Chem. A* **2021**, *9*, 11427–11432. [CrossRef]
52. Xu, H.; Zhang, Z.; Liu, J.; Do-Thanh, C.L.; Chen, H.; Xu, S.; Lin, Q.; Jiao, Y.; Wang, J.; Wang, Y.; et al. Entropy-stabilized single-atom Pd catalysts via high-entropy fluorite oxide supports. *Nat. Commun.* **2020**, *11*, 3908. [CrossRef]
53. Turbasu, S.; Dinesh, B.; Shiv, N.K. Developing efficient Suzuki cross-coupling catalysts by doping palladium clusters with silver. *ACS Catal.* **2021**, *11*, 11459–11468.
54. Beletskaya, I.P.; Cheprakov, A.V. Palladacycles in catalysis—A critical survey. *J. Organomet. Chem.* **2004**, *689*, 4055–4082. [CrossRef]

55. Chen, H.; Shuang, H.; Lin, W.; Li, X.; Zhang, Z.; Li, J.; Fu, J. Tuning interfacial electronic properties of palladium oxide on vacancy-abundant carbon nitride for low-temperature dehydrogenation. *ACS Catal.* **2021**, *11*, 6193–6199. [CrossRef]
56. Tao, X.; Long, R.; Wu, D.; Hu, Y.; Qiu, G.; Qi, Z.; Li, B.; Jiang, R.; Xiong, Y. Anchoring positively charged Pd single atoms in ordered porous ceria to boost catalytic activity and stability in Suzuki coupling reactions. *Small* **2020**, *16*, 2001782. [CrossRef]